

1 A direct comparison between field-measured

2 and sensor-based estimates of soil carbon

3 dioxide flux across six National Ecological

4 Observatory Network sites enabled by the

5 neonSoilFlux R package

6 John Zobitz¹ Ed Ayres² Zoey Werbin³ Ridwan Abdi¹

7 Natalie Ashburner-Wright⁴ Lillian Brown⁴

8 Ryan Frink-Sobierajski⁴ Lajntxiag Lee¹ Dijonë Mehmeti¹

9 Christina Tran⁴ Ly Xiong¹ Naupaka Zimmerman⁴

10 ¹ Augsburg University, 2211 Riverside Avenue, Minneapolis, MN 55454

11 ² National Ecological Observatory Network, 1685 38th Street, Suite 100, Boulder, CO 80301

12 ³ Boston University, 5 Cummington Street, Boston, MA 02215

13 ⁴ University of San Francisco, 2130 Fulton Street, San Francisco, CA 94117

¹⁴ **Acknowledgments**

¹⁵ JZ acknowledges Kathleen O'Rourke for code development. NZ thanks technical staff at
¹⁶ USF for support with field gear assembly and shipping. We thank the NEON field staff
¹⁷ and assignable assets teams for facilitating each of the six NEON site visits. We are grateful
¹⁸ to LI-COR technical staff for helpful discussions about optimal sampling methods. This work
¹⁹ was supported by NSF DEB grant #2017829 awarded to JZ, and NSF DEB grant #2017860
²⁰ awarded to NZ.

²¹ **Conflict of Interest Statements**

²² None of the authors have a financial, personal, or professional conflict of interest related to
²³ this work.

²⁴ **Author Contributions**

²⁵ Conceptualization: JZ, NZ; Methodology: EA, JZ, NZ; Software: JZ, NZ, ZW, E A, DM, RA,
²⁶ LX, LL; Validation: JZ, NZ; Formal Analysis: JZ, NZ, DM, RA, LX, LL; Investigation: JZ,
²⁷ NZ, RF-S, CT, NA-W, LB; Resources: JZ, NZ; Data curation: JZ, NZ, DM, LX; Writing
²⁸ – original draft: JZ, NZ; Writing – review and editing: JZ, NZ, ZW, EA, CT, DM, LX,;
²⁹ Visualization: JZ, NZ, DM, RA, LX; Supervision: JZ; NZ; Project Administration: JZ; NZ;
³⁰ Funding Acquisition: JZ; NZ

³¹ **Data Availability**

³² Data available from the Zenodo LINK <http://dx.doi.org/10.5061/dryad.41qh7> (Kiere & Drummond 2016)."

³⁴ **1 Abstract**

³⁵ A key component of constraining the uncertainty of the terrestrial carbon sink is quantification
³⁶ of terrestrial soil carbon fluxes, which vary across time and ecosystem type. One method for
³⁷ the estimation of these fluxes and their associated uncertainties is the flux gradient method,
³⁸ which can be calculated via a variety of existing approaches. Robust estimation of soil carbon
³⁹ fluxes on a sub-daily level requires measurements of soil CO₂ concentration, water content,
⁴⁰ temperature, and other environmental measurements and soil properties. These data are
⁴¹ publicly available from the National Ecological Observatory Network at sites spanning a range
⁴² of 20 different ecoclimatic domains across the continental United States, Puerto Rico, Alaska,
⁴³ and Hawai'i. We present an R software package (`neonSoilFlux`) that acquires NEON soil
⁴⁴ environmental data and computes soil carbon flux at a half-hourly time step at a user-specified
⁴⁵ NEON site and month in a tidy data format. To validate the computed fluxes, we visited six
⁴⁶ focal NEON sites and measured soil carbon fluxes using a closed-dynamic chamber approach.
⁴⁷ The validation confirmed that a primary challenge in reducing soil carbon flux uncertainty is
⁴⁸ correctly characterizing diffusivity and soil water content across the soil profile. Outputs from
⁴⁹ the `neonSoilFlux` package contribute to existing databases of soil carbon flux measurements,
⁵⁰ providing near real-time estimates of a critical component of the terrestrial carbon cycle.

⁵¹ **1.1 Keywords**

⁵² Soil carbon, carbon dioxide, flux gradient, carbon cycle, field validation, soil respiration, ecosys-
⁵³ tem variability, diffusion

⁵⁴ **2 Data for peer review**

⁵⁵ Anonymous data and code for peer review is available here: [LINK](#)

⁵⁶ **3 Introduction**

⁵⁷ Soils contain the largest reservoir of terrestrial carbon (Jobbágy & Jackson, 2000). A critical
⁵⁸ component of this reservoir is soil organic matter, the accumulation of which is influenced
⁵⁹ by biotic factors such as above-ground plant inputs (Jackson et al., 2017). These inputs in
⁶⁰ turn are influenced by environmental factors such as growing season length, temperature, and
⁶¹ moisture (Desai et al., 2022), which also affect the breakdown of soil organic matter and its
⁶² return to the atmosphere. Across heterogeneous terrestrial landscapes, the interplay between
⁶³ these biotic and abiotic factors influence the size of the soil contribution to the terrestrial
⁶⁴ carbon sink (Friedlingstein et al., 2023). However, the heterogeneity of these processes across
⁶⁵ diverse ecosystems in the context of rapid environmental change leads to large uncertainty in
⁶⁶ the magnitude of this sink in the future, and thus a pressing need to quantify changes in soil
⁶⁷ carbon pools and fluxes across scales.

⁶⁸ Ecological observation networks such as the United States' National Ecological Observatory
⁶⁹ Network (NEON) and others (e.g. FLUXNET or the Integrated Carbon Observation System)
⁷⁰ present a significant advancement in the nearly continuous observation of biogeochemical pro-
⁷¹ cesses at the continental scale. Notably, at 47 terrestrial sites across the continental United
⁷² States, NEON provides half-hourly measurements of soil CO₂ concentration, temperature,
⁷³ and moisture at different vertical depths. Each of these NEON sites also encompasses mea-
⁷⁴ surements of the cumulative sum of all ecosystem carbon fluxes in an airshed using the eddy
⁷⁵ covariance technique (Balderuppi, 2014). Soil observations provided by NEON are on the same

76 timescale and standardized with eddy covariance measurements from FLUXNET. These types
77 of nearly continuous observational data (NEON and FLUXNET) can be used to reconcile dif-
78 ferences between model-derived or data-estimated components of ecosystem carbon flux (Jian
79 et al., 2022; Luo et al., 2011; Phillips et al., 2017; J. Shao et al., 2015; P. Shao et al., 2013;
80 Sihi et al., 2016).

81 Estimated or observed soil carbon fluxes are a key metric for understanding change in soil
82 carbon pools over time (Bond-Lamberty et al., 2024). A soil carbon flux to the atmosphere
83 (F_S , units $\mu\text{mol m}^{-2} \text{s}^{-1}$), represents the aggregate process of transfer of soil CO_2 to the
84 atmosphere from physical and biological processes (e.g. diffusion and respiration). Soil carbon
85 fluxes can be assumed to encompass soil carbon respiration from autotrophic or heterotrophic
86 sources (Davidson et al., 2006), typically assumed to be static across the soil biome and
87 modeled with a exponential Q_{10} paradigm (Bond-Lamberty et al., 2004; Chen & Tian, 2005;
88 Hamdi et al., 2013).

89 One method by which F_S is measured in the field is through the use of soil chambers in a closed,
90 well-mixed system (Norman et al., 1997) with headspace trace gas concentrations measured
91 with an infrared gas analyzer (IRGA). F_S can also be estimated from soil CO_2 measurements
92 at different depths in the soil using the flux-gradient method (Maier & Schack-Kirchner, 2014).
93 This method is an approach that uses conservation of mass to calculate flux at a vertical soil
94 depth z at steady state by applying Fick's law of diffusion. A simplifying assumption for the
95 flux-gradient method is that there is no mass transfer in the other spatial dimensions x and y
96 (Maier & Schack-Kirchner, 2014). The diffusivity profile, a key component of this calculation,
97 varies across the soil depth as a function of soil temperature, soil volumetric water content,
98 atmospheric air pressure, and soil bulk density (Millington & Shearer, 1971; Moldrup et al.,
99 1999; Sallam et al., 1984).

100 Databases such as the Soil Respiration Database (SRDB) or the Continuous Soil Respiration

101 Database (COSORE) add to the growing network of resources for making collected observa-
102 tions of soil fluxes available to other workers (Bond-Lamberty, 2018; Bond-Lamberty et al.,
103 2020; Bond-Lamberty & Thomson, 2010; Jian et al., 2021; Jiang et al., 2024). However, these
104 databases currently encompass primarily direct soil measurements of fluxes (i.e. those using
105 methods like the closed-chamber method described above). Currently, NEON provides all
106 measurements to calculate F_S from Fick's law, but soil flux as a derived data product was
107 descoped from the initial network launch due to budget constraints (Berenbaum et al., 2015).
108 Deriving estimates of F_S using continuous sensor data across NEON sites thus represents a
109 high priority.

110 This study describes an R software package, `neonSoilFlux`, that can be used to derive a
111 standardized estimate of F_S at all terrestrial NEON sites. After calculating these flux estimates,
112 we then validated them against direct chamber-based field observations of soil carbon dioxide
113 flux from a subset of terrestrial NEON sites spanning six states.

114 Key objectives of this study are to:

- 115 1. Apply the flux-gradient method to estimate soil CO₂ flux from continuous sensor mea-
116 surements across NEON sites.
- 117 2. Benchmark estimated soil carbon fluxes against field measurements (e.g. direct chamber
118 measurements of soil flux).
- 119 3. Identify sources of error in the flux-gradient approach across diverse sites in order to
120 guide future work.

₁₂₁ **4 Materials and Methods**

₁₂₂ **4.1 Field methods**

₁₂₃ **4.1.1 Focal NEON Sites**

₁₂₄ In order to acquire field data to validate model predictions of flux, we selected six terrestrial
₁₂₅ NEON sites for analysis. We conducted field measurement campaigns at these sites, which
₁₂₆ span a range of environmental gradients and terrestrial domains (Table 1). SJER, SRER, and
₁₂₇ WREF were visited during May and June of 2022, and WOOD, KONZ, and UNDE during
₁₂₈ May and June of 2024.

₁₂₉ Over the course of two field campaigns in 2022 and 2024, we conducted week-long visits at
₁₃₀ each site. In consultation with NEON field staff, we first selected a specific plot in the soil
₁₃₁ sampling array to maximize the concurrent availability of sensor data.

₁₃₂ **4.1.2 Soil collar placement**

₁₃₃ Either one (2022 sampling campaign) or two (2024 sampling campaign) PVC soil collars (20.1
₁₃₄ cm inside diameter) were installed in close proximity to the permanent NEON soil sensors at
₁₃₅ each site (Figure 1). The soil plot where measurements were taken was chosen at each site
₁₃₆ in consultation with NEON staff to maximize likelihood of quality soil sensor measurements
₁₃₇ during the duration of the IRGA measurements at each site. After installation, collar(s) were
₁₃₈ left to equilibrate for approximately 24 hours prior to measurements being taken.

¹³⁹ **4.1.3 Infrared gas analyzer measurements of soil CO₂ flux**

¹⁴⁰ In 2022, we then made measurements of flux on an hourly interval for 8 hours each day.
¹⁴¹ Measurements were taken from roughly 8 am to 4 pm, with the time interval selected to
¹⁴² capture the majority of the diurnal gradient of soil temperature each day. These measurements
¹⁴³ were made using a LI-6800 infrared gas analyzer instrument (LI-COR Environmental, Lincoln,
¹⁴⁴ NE) fitted with a soil chamber attachment (attachment 6800-09). In 2024, we again used
¹⁴⁵ the same LI-6800 instrument, but made half-hourly measurements over an approximately 8
¹⁴⁶ hour period. In addition, we also installed a second collar and used a second instrument, an
¹⁴⁷ LI-870 CO₂ IRGA, connected to an automated robotic chamber (LI-COR chamber 8200-104)
¹⁴⁸ controlled by an LI-8250 multiplexer, to make automated measurements. The multiplexer was
¹⁴⁹ configured to take half-hourly measurements 24 hours a day for the duration of our sampling
¹⁵⁰ bout at each site. Each instrument was paired with a soil temperature and moisture probe
¹⁵¹ (Stevens HydraProbe, Stevens Water, Portland, OR) that was used to make soil temperature
¹⁵² and moisture measurements concurrent with the CO₂ flux measurements. Chamber volumes
¹⁵³ were set by measuring collar offsets at each site. System checks were conducted daily for the
¹⁵⁴ LI-6800 and weekly for the LI-8250. Instruments were factory calibrated before each field
¹⁵⁵ season.

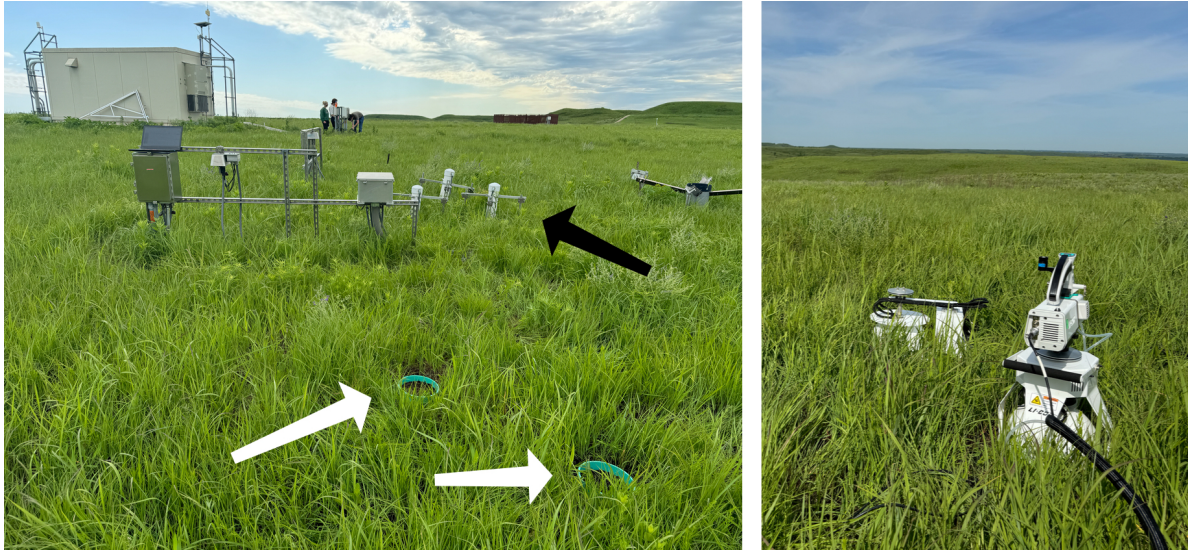


Figure 1: Spatial layout of field sampling using a closed-dynamic chamber setup at a representative NEON site (KONZ). Left image shows collars (white arrows) and permanent soil sensor installation (black arrow) and right image shows the LI-6800 (foreground) and LI-8200-104 (background) instruments placed on the collars.

Table 1: Listing of NEON sites studied for field work and analysis. $\overline{T_S}$: average soil temperature during field measurements. \overline{SWC} : average soil water content during field measurements. Soil plot refers to the particular location in the soil sensor array (denoted as HOR by NEON) where field measurements were made.

Site (NEON site ID)	Location	Ecosystem type	Mean annual tempera- ture	$\overline{T_S}$ (°)	Mean annual precipita- tion	\overline{SWC} (%)	Field measure- ment dates	Soil plot
Santa	31.91068,	Shrubland	19.3°C	47.6°	346 mm	4.0%	29 May	004
Rita	-						2024 - 01	
Experi- mental Range (SRER)	110.83549						June 2024	

Table 1: Listing of NEON sites studied for field work and analysis. \bar{T}_S : average soil temperature during field measurements. \bar{SWC} : average soil water content during field measurements. Soil plot refers to the particular location in the soil sensor array (denoted as HOR by NEON) where field measurements were made.

Site (NEON site ID)	Location	Ecosystem type	Mean annual tempera- ture	\bar{T}_S (°)	Mean annual precipita- tion	\bar{SWC} (%)	Field measure- ment dates	Soil plot
San Joaquin Experimental Range (SJER)	37.10878, -	Oak woodland	16.4°C	41.7°	540 mm	1.2%	01 June 2022 - 04	005
Wind River Experimental Forest (WREF)	45.82049, -	Evergreen forest	9.2°C	15.3°	2225 mm	27.2%	07 June 2022	001
Chase Lake National Wildlife Refuge (WOOD)	121.95191	Restored prairie	4.9°C	14.9°	495 mm	14.9%	03 June 2024 - 09	001
Konza Prairie Biological Station (KONZ)	47.1282, -	Tallgrass prairie	12.4°C	23.4°	870 mm	23.4%	29 May 2024 - 01	001
	99.241334	grassland					June 2024	
	96.563075						June 2024	

Table 1: Listing of NEON sites studied for field work and analysis. \bar{T}_S : average soil temperature during field measurements. \bar{SWC} : average soil water content during field measurements. Soil plot refers to the particular location in the soil sensor array (denoted as HOR by NEON) where field measurements were made.

Site (NEON site ID)	Location	Ecosystem type	Mean annual tempera- ture	\bar{T}_S (°)	Mean annual precipita- tion	\bar{SWC} (%)	Field measure- ment dates	Soil plot
University of Notre Dame Environ- mental Research Center (UNDE)	46.23391, - 89.537254	Deciduous forest	4.3°	13.0°	802 mm	13.0%	22 May 2024 - 25 May 2024	004

4.1.4 Post-collection processing of field data

We used LI-COR SoilFluxPro software (v 5.3.1) to assess the data after collection and to inform sampling parameters. We checked appropriateness of dead band and measurement durations using built-in evaluation tools. Based on this, the deadband period was set for 30-40 seconds, depending on the site, and the measurement duration was 180 seconds with a 30 second pre-purge and a 30 second post-purge at most sites, and a 90 sec pre- and post-purge at sites with higher humidity due to recent precipitation events. We also assessed the R^2 of linear and exponential model fits to measured CO_2 to verify measurement quality.

164 **4.2 neonSoilFlux R package**

165 We developed an R package (`neonSoilFlux`; <https://CRAN.R-project.org/package=neonSoilFlux>)
166 to compute half-hourly soil carbon fluxes and uncertainties from NEON data. The objective
167 of the `neonSoilFlux` package is a unified workflow (Figure 2) for soil data acquisition and
168 analysis that supplements the existing data acquisition R package `neonUtilities` (LINK TO
169 BE ADDED AFTER PEER REVIEW).

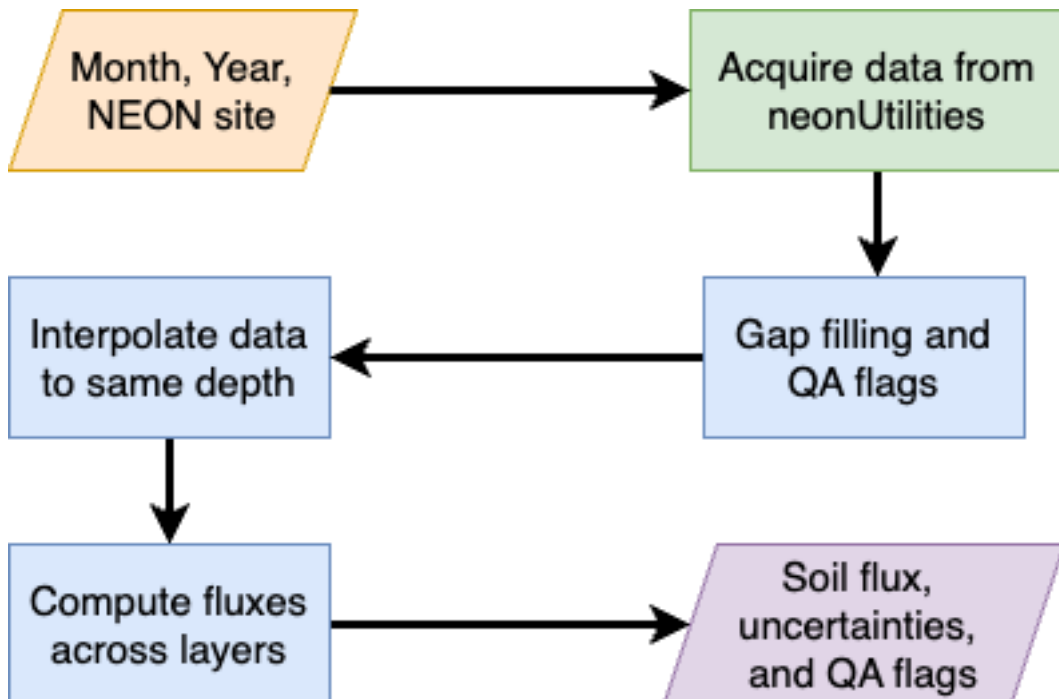


Figure 2: Diagram of `neonSoilFlux` R package. For a given month, year, and NEON site (orange parallelogram), the package acquires all relevant data to compute F_S using the `neonUtilities` R package (green rectangle). Data are gap-filled according to reported QA flags and interpolated to the same measurement depth before computing the soil flux, uncertainties, and final QA flags (blue rectangles). The package reports the associated soil flux, uncertainties, and quality assurance (QA) flags for the user (purple parallelogram).

170 At a given NEON observation there are five replicate soil plots, each with measurements of
171 soil CO_2 concentration, soil temperature, and soil moisture at different depths (Figure 3). The

172 `neonSoilFlux` package acquires measured soil water content (National Ecological Observatory
 173 Network (NEON), 2024e), soil CO₂ concentration (National Ecological Observatory Network
 174 (NEON), 2024b), barometric pressure from the nearby tower (National Ecological Observa-
 175 tory Network (NEON), 2024a), soil temperature (National Ecological Observatory Network
 176 (NEON), 2024d), and soil properties (e.g. bulk density) (National Ecological Observatory Net-
 177 work (NEON), 2024c). The static soil properties were collected from a nearby soil pit during
 178 site characterization and are assumed to be constant at each site.

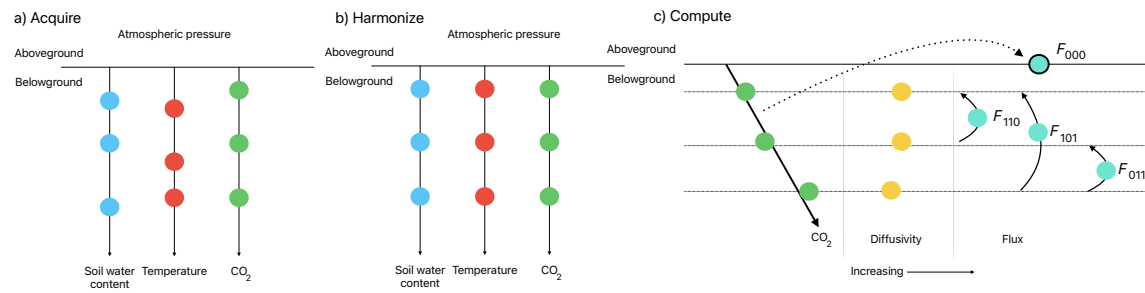


Figure 3: Model diagram for data workflow for the `neonSoilFlux` R package. a) Acquire: Data are obtained from given NEON location and horizontal sensor location, which includes soil water content, soil temperature, CO₂ concentration, and atmospheric pressure. All data are screened for quality assurance; if gap-filling of missing data occurs, it is flagged for the user. b) Any belowground data are then harmonized to the same depth as CO₂ concentrations using linear regression. c) The flux across a given depth is computed via Fick's law, denoted with F_{ijk} , where i , j , or k are either 0 or 1 denoting the layers the flux is computed across (i = closest to surface, k = deepest). F_{000} represents a flux estimate where the gradient dC/dz is the slope of a linear regression of CO₂ with depth.

179 The workflow to compute a value of F_S with `neonSoilFlux` consists of three primary steps,
 180 illustrated in Figure 3. First, NEON data are acquired for a given site and month via the
 181 `neonUtilities` R package (yellow parallelogram and green rectangle in Figure 2 and Panel a
 182 in Figure 3). Acquired environmental data can be exported to a comma separated value file
 183 for additional analysis. Quality assurance (QA) flags are reported as an indicator variable.
 184 The second step is harmonizing the data to compute soil fluxes across soil layers. This step

185 consists of three different actions (blue rectangles in Figure 2 and Panel b in Figure 3). If a
186 given observation by NEON is reported as not passing a quality assurance check, we applied
187 a gap filling method to replace that measurement with its monthly mean at that same depth
188 (Section 4.2.1). Belowground measurements of soil water and soil temperature are then inter-
189 polated to the same depth as soil CO₂ measurements. The diffusivity (Section 4.2.2) and soil
190 flux across different soil layers (Section 4.2.3) are then computed.

191 The third and final step is computing a surface soil flux through extrapolation to the sur-
192 face (purple parallelogram in Figure 2 and Panel c in Figure 3). Uncertainty on a soil flux
193 measurement is computed through quadrature. An aggregate quality assurance (QA) flag
194 for each environmental measurement is also reported, representing if any gap-filled measure-
195 ments were used in the computation of a soil flux. Within the soil flux-gradient method,
196 several different approaches can be used to derive a surface flux (Maier & Schack-Kirchner,
197 2014); the `neonSoilFlux` package reports four different possible values for soil surface flux
198 (Section 4.2.3).

199 4.2.1 Gap-filling routine

200 NEON reports QA flags as a binary value for a given measurement and half-hourly time inter-
201 val. We replaced any flagged measurements at a location's spatial depth z with a bootstrapped
202 sample of the monthly mean for all un-flagged measurements for that month. These measure-
203 ments are represented by the vector \mathbf{m} , standard errors σ , and the 95% confidence interval
204 (the so-called expanded uncertainty, Farrance & Frenkel (2012)) ϵ . All of these vectors have
205 length M . We have that $\vec{\sigma}_i \leq \vec{\epsilon}_i$. We define the bias as $\mathbf{b} = \sqrt{\epsilon^2 - \sigma^2}$.

206 We generate a vector of bootstrap samples of the distribution of the monthly mean \bar{m} and
207 monthly standard error $\bar{\sigma}$ the following ways:

- 208 1. Randomly sample from the uncertainty and bias independently: σ_j and the bias \mathbf{b}_k (not
 209 necessarily the same sample).
- 210 2. Generate a vector \mathbf{n} of length N , where \mathbf{n}_i is a random sample from a normal distribution
 211 with mean m_i and standard deviation σ_j . Since $M < N$, values from \mathbf{m} will be reused.
- 212 3. With these N random samples, $\bar{y}_i = \vec{x} + \vec{b}_k$ and s_i is the sample standard deviation of \vec{x} .
 213 We expect that $s_i \approx \vec{\sigma}_j$.
- 214 4. The reported monthly mean and standard deviation are then computed $\bar{\bar{y}}$ and \bar{s} . Measurements and uncertainties that did not pass the QA check are then substituted with
 215 $\bar{\bar{y}}$ and \bar{s} .

217 This gap-filling method described here provides a consistent approach for each data stream,
 218 however we recognize that other gap-filling alternatives may be warranted for longer-term gaps
 219 (e.g. such as correlations with other NEON measurement levels and soil plots), or measure-
 220 ment specific gap-filling routines. We discuss the effect of gap-filling on our measurements in
 221 Section 6.

222 **4.2.2 Soil diffusivity**

223 Soil diffusivity D_a at a given measurement depth is the product of the diffusivity in free air
 224 $D_{a,0}$ ($\text{m}^2 \text{ s}^{-1}$) and the tortuosity ξ (no units) (Millington & Shearer, 1971).

225 We compute $D_{a,0}$ with Equation 1:

$$D_{a,0} = 0.0000147 \cdot \left(\frac{T_i + 273.15}{293.15} \right)^{1.75} \cdot \left(\frac{P}{101.3} \right) \quad (1)$$

226 where T_i is soil temperature ($^{\circ}\text{C}$) at depth i (National Ecological Observatory Network
227 (NEON), 2024d) and P surface barometric pressure (kPa) (National Ecological Observatory
228 Network (NEON), 2024a).

229 Previous studies by Sallam et al. (1984) and Tang et al. (2003) demonstrated the sensitivity
230 of modeled F_S depending on the tortuosity model used to compute diffusivity. At low soil
231 water content, the choice of tortuosity model may lead to order of magnitude differences in
232 D_a , which in turn affect modeled F_S . The `neonSoilFlux` package uses two different models
233 for ξ , representing the extremes reported in Sallam et al. (1984). The first approach uses the
234 Millington-Quirk model for diffusivity, Equation 2 (Millington & Shearer, 1971):

$$\xi = \frac{(\phi - SWC_i)^{10/3}}{\phi^2} \quad (2)$$

235 In Equation 2, SWC is the soil water content at depth i (National Ecological Observatory
236 Network (NEON), 2024e) and ϕ is the porosity (Equation 3), which in turn is a function of
237 soil physical properties (National Ecological Observatory Network (NEON), 2024c):

$$\phi = \left(1 - \frac{\rho_s}{\rho_m}\right) (1 - f_V) \quad (3)$$

238 In Equation 3, ρ_m is the particle density of mineral soil (2.65 g cm^{-3}), ρ_s the soil bulk density
239 (g cm^{-3}) excluding coarse fragments greater than 2 mm (National Ecological Observatory
240 Network (NEON), 2024c). The term f_V is a site-specific value that accounts for the proportion
241 of soil fragments between 2-20 mm. Soil fragments greater than 20 mm were not estimated
242 due to limitations in the amount of soil that can be analyzed (National Ecological Observatory
243 Network (NEON), 2024c). We assume there are no pores within rocks.

²⁴⁴ The second approach to calculate ξ is the Marshall model (Marshall, 1959), where $\xi = \phi^{1.5}$,
²⁴⁵ with ϕ defined from Equation 3.

²⁴⁶ **4.2.3 Soil flux computation**

²⁴⁷ We applied Fick's law (Equation 4) to compute the soil flux F_{ij} ($\mu\text{mol m}^{-2} \text{s}^{-1}$) across two
²⁴⁸ soil depths i and j :

$$F_{ij} = -D_a \frac{dC}{dz} \quad (4)$$

²⁴⁹ where D_a is the diffusivity ($\text{m}^2 \text{s}^{-1}$) and $\frac{dC}{dz}$ is the gradient of CO₂ molar concentration
²⁵⁰ ($\mu\text{mol m}^{-3}$, so the gradient has units of $\mu\text{mol m}^{-3} \text{m}^{-1}$). The soil surface flux is theoretically
²⁵¹ defined by applying Equation 4 to measurements collected at the soil surface and directly
²⁵² below the surface. Measurements of soil temperature, soil water content, and soil CO₂ molar
²⁵³ concentration across the soil profile allow for application of Equation 4 across different soil
²⁵⁴ depths. Each site had three measurement layers, so we denote the flux between which two
²⁵⁵ layers as a three-digit subscript F_{ijk} with indicator variables i , j , and k indicate if a given
²⁵⁶ layer was used (written in order of increasing depth), according to the following:

- ²⁵⁷ • F_{000} is a surface flux estimate using the intercept of the linear regression of D_a with
²⁵⁸ depth and the slope from the linear regression of CO₂ with depth (which represents $\frac{dC}{dz}$
²⁵⁹ in Fick's Law). Tang et al. (2003) used this approach to compute fluxes in an oak-grass
²⁶⁰ savannah.
- ²⁶¹ • F_{110} , F_{011} are fluxes across the two most shallow layers and two deepest layers respec-
²⁶² tively. The diffusivity used in Fick's Law is always at the deeper measurement layer.

When used as a surface flux estimate we assume CO₂ remains constant above this flux depth.

- F_{101} is a surface flux estimate using linear extrapolation using concentration measurements between the shallowest and deepest measurement layer. Hirano et al. (2003) and Tang et al. (2005) used an approach similar to F_{101} in a temperate deciduous broadleaf forest and ponderosa pine forest respectively.

Uncertainty in all F_{ijk} is computed through quadrature (Taylor, 2022).

4.3 Post processing evaluation

Following collection of field measurements and calculation of the soil fluxes from `neonSoilFlux` package, we compared measured F_S based on closed-dynamic chamber measurements with the LI-COR instruments to a given soil flux calculation from `neonSoilFlux` for each site and flux computation method. Statistics included the associated R² value, root mean squared error (RMSE), and signal to noise ratio (SNR), defined as the ratio of a modeled soil flux (F_{ijk}) from `neonSoilFlux` to its quadrature uncertainty (σ_{ijk}).

We observed that the range of values (e.g. $F_{ijk} \pm \sigma_{ijk}$) was much larger than the measured field flux. We evaluated $|F_S - F_{ijk}| < (1 - \epsilon)\sigma_{ijk}$, where F_S is a measured field soil flux from the LI-COR 6800 (as the LI-COR 870/8250 was used at only three sites in 2024 but the 6800 was used at all sites in both years). The parameter ϵ was an uncertainty reduction factor to evaluate how much the quadrature uncertainty could be reduced while maintaining precision between modeled F_{ijk} and measured F_S .

Finally, for a half-hourly interval we also computed a *post hoc* D_a using the LI-COR flux along with the CO₂ surface gradient reported by NEON using the measurement levels closest to the surface.

286 **5 Results**

287 Our overall goal was to design and validate an R package to estimate soil carbon dioxide
288 fluxes fluxes across terrestrial NEON sites using the flux gradient method. Validation of the
289 approach was based on comparison of estimated fluxes to field measurements made at six
290 focal sites. We first present our field measurement results, then the concordance between the
291 modeled and measured results, and lastly assess the factors that influenced the success of the
292 modeled approach at a given site.

293 **5.1 Field measurements**

294 We visited six NEON sites in the summers of 2022 and 2024. Using a closed-dynamic chamber
295 approach, we quantified soil carbon dioxide fluxes over the course of a week at each site. The
296 sites we visited ranged substantially in both their annual average temperature and precipitation
297 as well as their biome type (Table 2). These differences also influenced the wide range of
298 observed flux rates across sites. We used a LI-6800 to take manual hourly measurements at
299 the sites we visited in 2022 (SRER, SJER, WREF) and half-hourly manual measurements for
300 the sites we visited in 2024 (UNDE, KONZ, WOOD). In 2024 we also used an automated
301 chamber system (LI-870/LI-8250) to take half-hourly measurements 24 hours a day, thereby
302 also capturing nighttime fluxes in addition to the daytime fluxes also measured with the LI-
303 6800.

304 **5.2 Concordance between modelled and measured soil CO₂ flux**

305 The timeseries of the measured fluxes from the LI-COR 6800 and 870/8250 were compared
306 to modeled soil fluxes from the `neonSoilFlux` R package (Figure 4). We also assessed year-

Table 2: Summary of measured soil characteristics and flux results from field measurements across six NEON sites using a LI-COR 6800 (LI-870/8250 measurements omitted to enable direct comparability) via the closed-dynamic chamber method. Numeric values for soil CO₂ flux, soil temperature, and volumetric soil water content (VSWC) are the mean and standard deviation of field measurements at each site.

Site	Flux μmol m ⁻² s ⁻¹	Soil temp °C	VSWC cm ³ cm ⁻³	n
UNDE	2.55 ± 0.26	14.33 ± 0.77	0.33 ± 0.02	61
WOOD	3.02 ± 0.4	16.01 ± 1.54	0.28 ± 0.01	53
WREF	3.62 ± 0.3	15.34 ± 1.76	0.27 ± 0.06	21
KONZ	6.35 ± 0.97	27.28 ± 4.14	0.37 ± 0.01	44
SJER	0.94 ± 0.02	41.68 ± 11.22	0.01 ± 0.01	32
SRER	0.72 ± 0.09	47.64 ± 7.46	0.04 ± 0.01	32

long estimated flux time series and compared those to field measurements made at each site (Figure 5). Results are reported in local time. Where applicable, sites are displayed from left to right by increasing soil temperature (Table 1). Positive values of the flux indicate that there is a flux moving towards the surface. Overall, with the exception of SRER (discussed later) the computed fluxes determined using a variety of plausible methods spanned the field-measured fluxes, but the flux-gradient method that best approximated field measurements varied by site.

We compared statistics of the modeled soil fluxes to field F_S at each site (Table 3). As `neonSoilFlux` models half-hourly fluxes, we considered all measured fluxes over the duration of the half-hourly interval when computing the normalized root mean square error (NRMSE), R^2 , at each of the flux methods (F_{000} , F_{110} , F_{011} , F_{101}) for the diffusivity models studied (Millington-Quirk or Marshall).

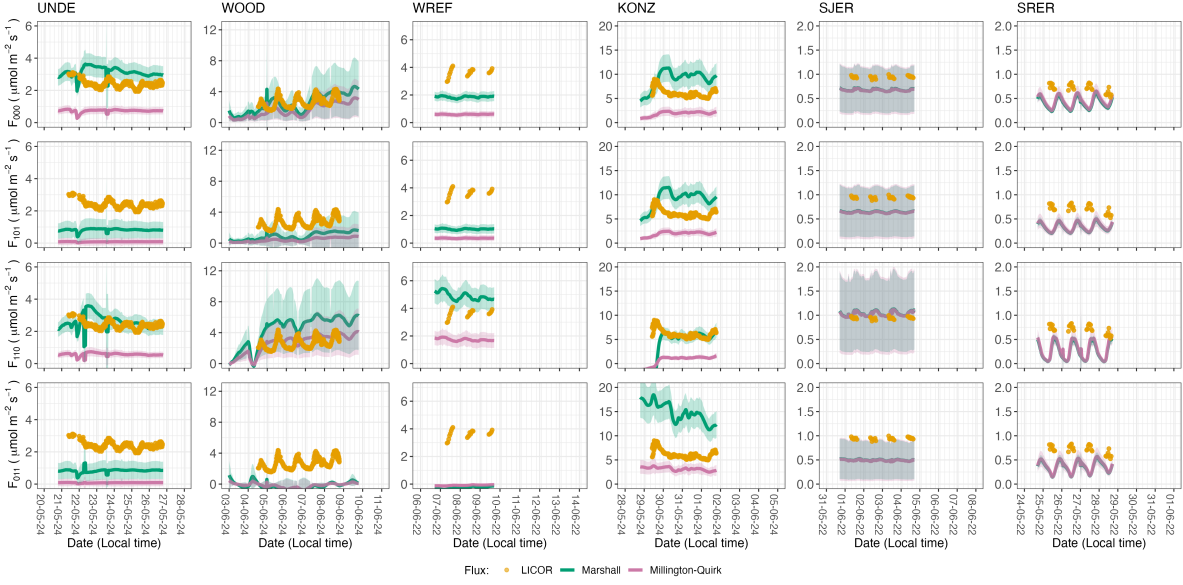


Figure 4: Timeseries of both measured F_S (yellow circles) and modeled soil fluxes (green or purple lines) by the `neonSoilFlux` R package. Fluxes from the `neonSoilFlux` R package are separated by the diffusivity model used (Millington-Quirk or Marshall, Section 4.2.2). Vertical axis labels in the first column represent the measurement levels where the flux-gradient approach is applied (Section 4.2.3). Ribbons for modeled soil fluxes represent ± 1 standard deviation. Results are reported in local time.

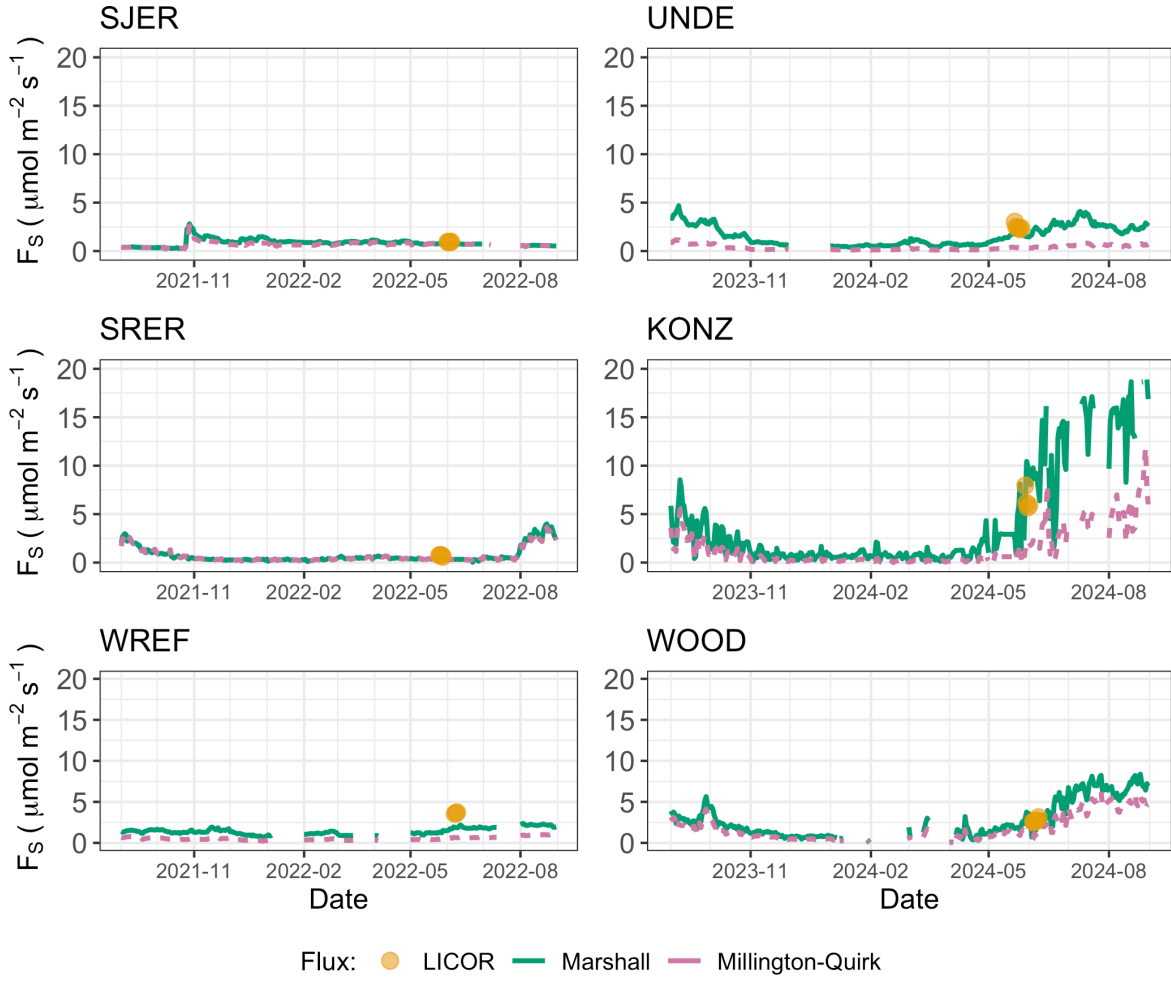


Figure 5: Timeseries of both daily-averaged field F_S (yellow circles) and daily ensemble averaged soil fluxes (average of F_{000} , F_{101} , F_{011} , F_{110} , Section 4.2.3) by the `neonSoilFlux` R package, separated by the diffusivity model used (green or purple lines, Millington-Quirk or Marshall, Section 4.2.2).

Table 3: Reported statistics from the model fits.

	Millington-Quirk		Marshall	
	NRMSE	R2	NRMSE	R2
KONZ				
F_{110}	0.87	0.41	0.63	0.41
F_{101}	0.69	0.22	0.60	0.15
F_{011}	0.52	0.20	1.35	0.25
F_{000}	0.70	0.23	0.58	0.14
SJER				
F_{110}	0.13	0.17	0.14	0.18
F_{101}	0.32	0.21	0.31	0.24
F_{011}	0.49	0.02	0.48	0.03
F_{000}	0.29	0.17	0.28	0.18
SRER				
F_{110}	0.56	0.00	0.59	0.00
F_{101}	0.66	0.53	0.67	0.52
F_{011}	0.69	0.49	0.70	0.49
F_{000}	0.58	0.51	0.61	0.51
UNDE				
F_{110}	0.77	0.06	0.25	0.02
F_{101}	0.97	0.10	0.66	0.14
F_{011}	0.97	0.05	0.66	0.04
F_{000}	0.70	0.16	0.36	0.06
WOOD				
F_{110}	0.31	0.10	0.97	0.06
F_{101}	0.87	0.16	0.69	0.13
F_{011}	1.12	0.10	1.24	0.11
F_{000}	0.47	0.16	0.36	0.15
WREF				
F_{110}	0.53	0.78	0.35	0.75
F_{101}	0.91	0.24	0.73	0.35
F_{011}	1.03	0.37	1.07	0.37
F_{000}	0.84	0.00	0.49	0.05

319 **5.3 Assessment of data gaps**

320 For a given half-hourly time period, the `neonSoilFlux` package assigns a QA flag for a mea-
 321 surement if more than one values across all measurement depths uses gap-filled data (Section 4.2.1).
 322 Panel a of Figure 6 reports the proportion of gap-filled data for all input environmental mea-
 323 surements at each site during the period when field measurements were made. Soil fluxes are
 324 computed from 4 different types of input measurements (T_S , SWC , P , and CO_2), any of which
 325 could have a QA flag in a half-hourly interval. Panel b of Figure 6 displays at each site the
 326 distribution of the number of different gap-filled measurements used to compute a half-hourly
 327 flux. The largest cause of measurements needing to be gap-filled was missing or flagged soil
 328 moisture data. SJER and WOOD required the largest number of gap-filled measurements,
 329 which were primarily SWC and T_S .

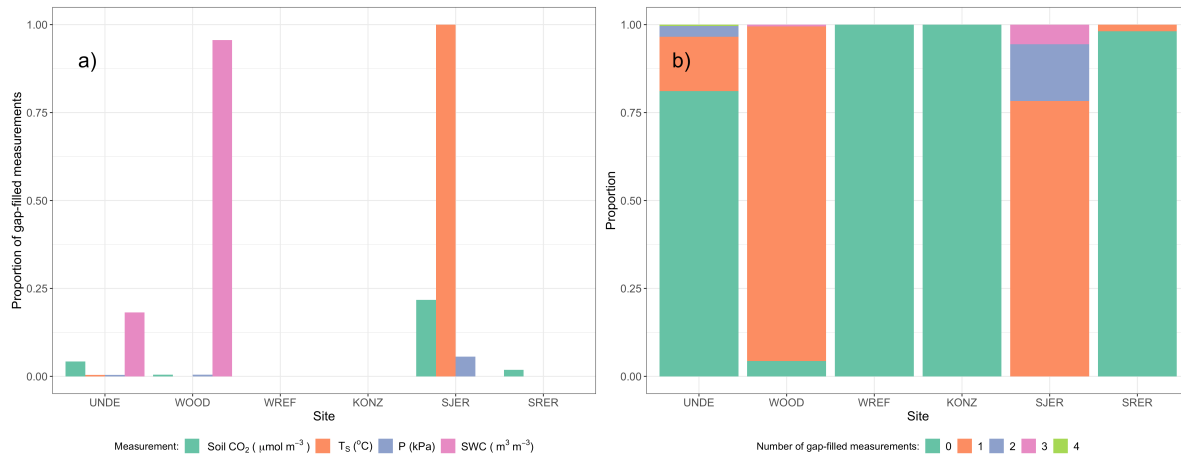


Figure 6: Panel a) Proportion of input gap-filled environmental measurements used to generate F_S from the `neonSoilFlux` package, by study site. Panel b) distribution of the usage of gap-filled measurements at each site.

330 **5.4 Assessing the signal to noise ratio (SNR) and evaluating estimated
331 uncertainties**

332 The computed signal to noise ratio (SNR) and the proportion of measured field fluxes within
333 the modeled uncertainty for a given flux computation method F_{ijk} suggest that there was
334 substantial variability in the agreement between the gradient method and field-measured ob-
335 servations (Figure 7, Section 4.3). Here, values of SNR greater than unity indicates lower
336 reported uncertainty, as propogated by quadrature due to a relatively higher precision of
337 measured input variables (CO_2 , T_S , SWC , or P).

338 The sensitivity to an uncertainty reduction factor (ϵ , bottom panels in Figure 7) demonstrates
339 how concordance between measured and modeled fluxes would be affected if modeled uncer-
340 tainty σ_{ijk} decreases. As ϵ increases from left to right in each figure, the possible range of
341 values for each predicted flux value decreases and the proportion of measured fluxes that fall
342 within that range also decreases.

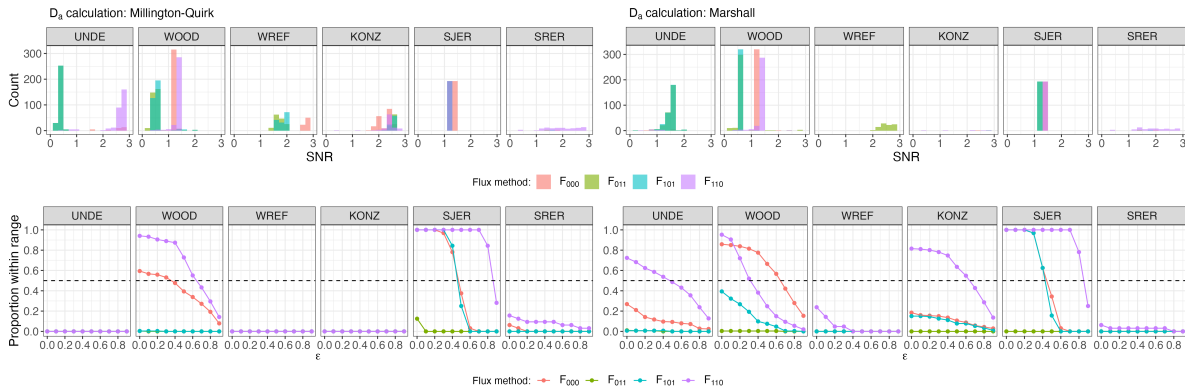


Figure 7: Top panels: distribution of SNR values across each of the different sites for modeled effluxes from the `neonSoilFlux` package, depending on the diffusivity calculation used (Millington-Quirk or Marshall, Section 4.2.2). Bottom panels: Proportion of measured F_S within the modeled range of a flux computation method F_{ijk} given an uncertainty reduction factor ϵ , or $|F_S - F_{ijk}| < (1 - \epsilon)\sigma_{ijk}$.

343 **5.5 Effects of method choice on diffusivity estimates**

344 Figure 8 reports the distribution of D_a (from both the Marshall and Millington-Quirk methods,
345 Section 4.2.2) at each study site, and the *post hoc* computation of D_a (Section 4.2.2). Over
346 the course of a half-hourly interval the same CO₂ gradient (from neonSoilFlux) was used for
347 the different LICOR measured fluxes. We only used F_S measured by the LICOR 6800 at all
348 sites to standardize comparisons. For the field-estimated measurements we omitted negative
349 values of D_a , as that indicates the CO₂ gradient decreases with soil depth (thereby violating
350 assumptions of the flux-gradient method).

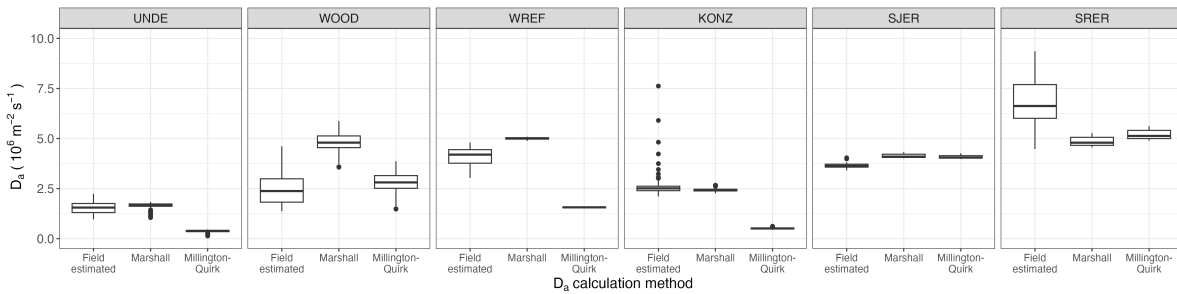


Figure 8: Distribution of diffusivity (D_a) at each study site. Values of D_a were provided by the neonSoilFlux package, computed from the Millington-Quirk or Marshall models (Section 4.2.2). A post-hoc estimate of diffusivity (labeled as “Field estimated”) was computed through the field measured flux (Figure 4), divided by the CO₂ gradient from the measurement levels closest to the soil surface, as reported by NEON.

351 **6 Discussion**

352 This study presents a unified data science workflow to efficiently process automated measure-
353 ments of belowground soil CO₂ concentrations, water, and temperature to infer estimates of
354 soil surface CO₂ effluxes through application of Fick’s Law (Equation 4). Our core goals in this
355 study were: (1) to generate estimates of soil flux from continuous soil sensor data at terrestrial

356 NEON sites using the flux-gradient method and then (2) to compare those estimates to field-
357 measured fluxes based on the closed chamber approach at six NEON focal sites. We discuss
358 our progress toward these core goals through (1) an overall evaluation of the flux-gradient ap-
359 proach (and uncertainty calculation) and (2) site-specific evaluation of differences in estimated
360 vs measured fluxes.

361 **6.1 General evaluation of flux-gradient approach**

362 Key assumptions of the flux-gradient approach are that CO₂ concentrations increase through-
363 out the soil profile. Periods where this gradient condition are not met generally are connected
364 to biophysical processes such soil wetting events (e.g. KONZ), which have the effect of reduc-
365 ing the soil respiration or efflux due to a temporary reduction in diffusivity. When modeling
366 soil respiration, typically a non-linear response function that also considers soil type is used
367 (Bouma & Bryla, 2000; Yan et al., 2016, 2018). For the `neonSoilFlux` package, soil type is
368 connected to the bulk density, which was characterized at each NEON site based on replicate
369 samples collected from the site megapit at a subset of soil horizons, with an estimated un-
370 certainty of ±5% (see NEON User Guide to Soil physical and chemical properties, Megapit
371 (DP1.00096.001)). Coarse fragment estimates also have very large uncertainties, but because
372 the volume fraction tends to be low in surface soils it probably wouldn't contribute much
373 additional flux uncertainty.

374 The largest source of uncertainty to improve reliability of the flux estimate is to prevent the
375 usage of gap-filled data. Three sites (KONZ, SRER, and KONZ) had more than 75% of half-
376 hourly periods with no-gap filled measurements. Two sites (SJER and WOOD) had more
377 than 75% of half-hourly intervals with just one gap-filled measurement. While WREF re-
378 ported no gap-filled measurements, field data collection occurred following a once-in-a century
379 rainstorm with soils observed at their water holding capacity. We recommend that whenever

380 available, local field knowledge is supplementary to any QA filtering protocol of fluxes from
381 the `neonSoilFlux` package.

382 We recognize that this gap-filling approach may lead to gap-filled values that are quite different
383 from the actual values, such as an underestimate of soil moisture following rain events. Further
384 extensions of the gap filling method could use more sophisticated gap-filling routines, similar to
385 what is used for net ecosystem carbon exchange (Falge et al., 2001; Liu et al., 2023; Mariethoz
386 et al., 2015; Moffat et al., 2007; Zhang et al., 2023). The current gap-filling routine provides
387 a consistent approach that can be applied to each data stream, but further work may explore
388 alternative gap-filling approaches.

389 Based on this approach, we would *a priori* expect $F_{011} \leq F_{101} \leq F_{110} \leq F_{000}$ because the
390 previous flux estimates ones correspond to deeper depths which will could miss CO₂ produced
391 in shallower layers. Additionally, field flux measurements should correlate with F_{000} because
392 they represent surface fluxes.

393 6.2 Evaluation of flux-gradient approach at each site

394 Derived results from the `neonSoilFlux` package have patterns that are consistent, and com-
395 parable, to those directly measured to the field (Figure 4 and Figure 5). The advantage to
396 the `neonSoilFlux` package is the calculation of fluxes across different measurement depths, al-
397 lowing for additional site-specific customization. Here application of the flux-gradient method
398 provides a baseline estimate of soil fluxes that could be complemented through additional field
399 measurements (e.g. LICOR).

400 The six sites studied provide separate case studies for considerations when applying the flux-
401 gradient method to evaluate resulting uncertainties and fluxes For example, SRER is charac-
402 terized by sandy soil, which also led to the highest observed field soil temperatures. At SRER

403 the flux across the top two layers (F_{110}) produced a pattern of soil flux consistent with the ob-
404 served field data. The remaining methods F_{101} , F_{011} , or F_{000} are derived from information at
405 the deeper layer, which is decoupled both in terms of temperature and CO₂ concentration.

406 In addition, KONZ is a site that experienced a significant rain event prior to sampling with
407 eventual drying out over the course of the experiment. In this case we observed storage of soil
408 water which increased the soil CO₂ at the top layer, leading to negative values of flux at the
409 start of the experiment, with the fluxes drying out afterwards. In this case only when the soil
410 dried out (or returned to a baseline level), that the fluxes at the provided layer would work
411 out in this case.

412 When considering systematic deployment of this method across a measurement network, we
413 faced a number of independent challenges for consideration. Figure 7 illustrates tradeoffs
414 between (1) accuracy for modeled fluxes (defined here as closeness to field-measured F_S and
415 the uncertainty reduction factor ϵ), (2) precision (defined by the SNR), and (3) the choice of
416 the diffusivity model (Section 4.2.2) or flux computation method (Section 4.2.3). There was no
417 predictable pattern in SNR for either the flux computation method or diffusivity calculation,
418 indicating that output uncertainty is driven primarily by input measurement uncertainty (T_S ,
419 P , SWC, or CO₂). Across the different flux computation methods, the proportion of measured
420 fluxes where $|F_S - F_{ijk}| < (1-\epsilon)\sigma_{ijk}$ decreased as ϵ increased, except where field F_S was already
421 outside of the modeled range (i.e. UNDE and WREF). The method F_{110} (where soil flux was
422 computed from the top two soil layers) was the least sensitive to the uncertainty reduction
423 factor (ϵ). This lack of sensitivity could represent that the LICOR samples from the top
424 surface layer, and is most closely related to assumptions of the F_{110} method.

425 Comparing diffusivity methods to field estimated diffusivity (Figure 8) highlights the sensitivity
426 of F_{ijk} to diffusivity. Site-specific differences reflect the soil moisture availability across the
427 site (Table 1), and also reflect the model variation in Figure 4. While here we compare two

428 approaches to calculated diffusivity (Millington-Quirk or Marshall model), other diffusivity
429 models (e.g. the Moldrup model Moldrup et al. (1999)) could be evaluated. Ultimately the
430 choice of a particular diffusivity model could be determined through site-specific evaluated or
431 a source of model output uncertainty (e.g. as a model ensemble average).

432 **6.3 Recommendations for future method development**

433 The `neonSoilFlux` package provides three different approaches of values for a soil flux. We
434 believe these approaches reflect a variety of site-specific determination and assumptions used
435 to generate a soil flux measurement (Maier & Schack-Kirchner, 2014), with the choice of
436 method having a determinative approach on reported values. Reported results could further
437 be distilled down using ensemble averaging approaches (Elshall et al., 2018; Raftery
438 et al., 2005).

439 These challenges notwithstanding, the method used here and made available in the
440 `neonSoilFlux` R package has the potential to produce nearly continuous estimates of flux
441 across all terrestrial NEON sites. These estimates are a significant improvement on available
442 approaches to constrain the portion of ecosystem respiration attributable to the soil. This, in
443 turn, aids in our ability to understand the components of net ecosystem flux assessed at these
444 sites using the co-located eddy flux towers.

- 445 • Refine estimates to provide a realistic constraint on surface concentration measurements,
446 thereby increasing the gradient.
- 447 • Apply machine learning algorithms (e.g. random trees) or model averaging techniques to
448 generate a single flux estimate across each sites spatial location
- 449 • Benchmarking flux results to estimates provided by net ecosystem carbon exchange.

450 **7 Conclusions**

- 451 We have here presented an R package `neonSoilFlux` for the estimation of soil CO₂ fluxes from
452 continuous buried soil sensor measurements across terrestrial National Ecological Observatory
453 Network sites. We compared the predicted fluxes to those measured directly using a field-based
454 closed chamber approach. We find that...
- 455 Baldocchi, D. (2014). Measuring fluxes of trace gases and energy between ecosystems and the
456 atmosphere - the state and future of the eddy covariance method. *Global Change Biology*,
457 20(12), 3600–3609. <https://doi.org/10.1111/gcb.12649>
- 458 Berenbaum, M. R., Carpenter, S. R., Hampton, S. E., Running, S. W., & Stanzione, D. C.
459 (2015). *Report from the NSF BIO Advisory Committee Subcommittee on NEON Scope*
460 *Impacts*.
- 461 Bond-Lamberty, B. (2018). New Techniques and Data for Understanding the Global Soil Res-
462piration Flux. *Earth's Future*, 6(9), 1176–1180. <https://doi.org/10.1029/2018EF000866>
- 463 Bond-Lamberty, B., Ballantyne, A., Berryman, E., Fluet-Chouinard, E., Jian, J., Morris, K.
464 A., Rey, A., & Vargas, R. (2024). Twenty Years of Progress, Challenges, and Opportuni-
465ties in Measuring and Understanding Soil Respiration. *Journal of Geophysical Research:*
466 *Biogeosciences*, 129(2), e2023JG007637. <https://doi.org/10.1029/2023JG007637>
- 467 Bond-Lamberty, B., Christianson, D. S., Malhotra, A., Pennington, S. C., Sihi, D., AghaK-
468 ouchak, A., Anjileli, H., Altaf Arain, M., Armesto, J. J., Ashraf, S., Ataka, M., Baldocchi,
469 D., Andrew Black, T., Buchmann, N., Carbone, M. S., Chang, S.-C., Crill, P., Curtis, P.
470 S., Davidson, E. A., ... Zou, J. (2020). COSORE: A community database for continuous
471 soil respiration and other soil-atmosphere greenhouse gas flux data. *Global Change Biology*,
472 26(12), 7268–7283. <https://doi.org/10.1111/gcb.15353>
- 473 Bond-Lamberty, B., & Thomson, A. (2010). A global database of soil respiration data. *Bio-*
474 *geosciences*, 7(6), 1915–1926. <https://doi.org/10.5194/bg-7-1915-2010>

- 475 Bond-Lamberty, B., Wang, C., & Gower, S. T. (2004). A global relationship between the
476 heterotrophic and autotrophic components of soil respiration? *Global Change Biology*,
477 10(10), 1756–1766. <https://doi.org/10.1111/j.1365-2486.2004.00816.x>
- 478 Bouma, T. J., & Bryla, D. R. (2000). On the assessment of root and soil respiration for soils
479 of different textures: Interactions with soil moisture contents and soil CO₂ concentrations.
480 *Plant and Soil*, 227(1), 215–221. <https://doi.org/10.1023/A:1026502414977>
- 481 Chen, H., & Tian, H.-Q. (2005). Does a General Temperature-Dependent Q10 Model of Soil
482 Respiration Exist at Biome and Global Scale? *Journal of Integrative Plant Biology*, 47(11),
483 1288–1302. <https://doi.org/10.1111/j.1744-7909.2005.00211.x>
- 484 Davidson, E. A., Janssens, I. A., & Luo, Y. (2006). On the variability of respiration in
485 terrestrial ecosystems: Moving beyond Q10. *Global Change Biology*, 12, 154–164. <https://doi.org/10.1111/j.1365-2486.2005.01065.x>
- 486 Desai, A. R., Murphy, B. A., Wiesner, S., Thom, J., Butterworth, B. J., Koupaei-Abyazani, N.,
487 Muttaqin, A., Paleri, S., Talib, A., Turner, J., Mineau, J., Merrelli, A., Stoy, P., & Davis,
488 K. (2022). Drivers of Decadal Carbon Fluxes Across Temperate Ecosystems. *Journal of
489 Geophysical Research: Biogeosciences*, 127(12), e2022JG007014. <https://doi.org/10.1029/2022JG007014>
- 490 491
- 492 Elshall, A. S., Ye, M., Pei, Y., Zhang, F., Niu, G.-Y., & Barron-Gafford, G. A. (2018). Relative
493 model score: A scoring rule for evaluating ensemble simulations with application to micro-
494 bial soil respiration modeling. *Stochastic Environmental Research and Risk Assessment*,
495 32(10), 2809–2819. <https://doi.org/10.1007/s00477-018-1592-3>
- 496 Falge, E., Baldocchi, D., Olson, R., Anthoni, P., Aubinet, M., Bernhofer, C., Burba, G.,
497 Ceulemans, R., Clement, R., Dolman, H., Granier, A., Gross, P., Grünwald, T., Hollinger,
498 D., Jensen, N.-O., Katul, G., Keronen, P., Kowalski, A., Lai, C. T., ... Wofsy, S. (2001).
499 Gap filling strategies for defensible annual sums of net ecosystem exchange. *Agricultural
500 and Forest Meteorology*, 107(1), 43–69. [https://doi.org/10.1016/S0168-1923\(00\)00225-2](https://doi.org/10.1016/S0168-1923(00)00225-2)

- 501 Farrance, I., & Frenkel, R. (2012). *Uncertainty of Measurement: A Review of the Rules*
502 *for Calculating Uncertainty Components through Functional Relationships.* *The Clinical*
503 *Biochemist Reviews*, 33(2), 49–75.
- 504 Friedlingstein, P., O’Sullivan, M., Jones, M. W., Andrew, R. M., Bakker, D. C. E., Hauck,
505 J., Landschützer, P., Le Quéré, C., Luijkx, I. T., Peters, G. P., Peters, W., Pongratz, J.,
506 Schwingshackl, C., Sitch, S., Canadell, J. G., Ciais, P., Jackson, R. B., Alin, S. R., Anthoni,
507 P., ... Zheng, B. (2023). Global Carbon Budget 2023. *Earth System Science Data*, 15(12),
508 5301–5369. <https://doi.org/10.5194/essd-15-5301-2023>
- 509 Hamdi, S., Moyano, F., Sall, S., Bernoux, M., & Chevallier, T. (2013). Synthesis analysis
510 of the temperature sensitivity of soil respiration from laboratory studies in relation to
511 incubation methods and soil conditions. *Soil Biology and Biochemistry*, 58, 115–126. <https://doi.org/10.1016/j.soilbio.2012.11.012>
- 513 Hirano, T., Kim, H., & Tanaka, Y. (2003). Long-term half-hourly measurement of soil CO₂
514 concentration and soil respiration in a temperate deciduous forest. *Journal of Geophysical*
515 *Research: Atmospheres*, 108(D20). <https://doi.org/10.1029/2003JD003766>
- 516 Jackson, R. B., Lajtha, K., Crow, S. E., Hugelius, G., Kramer, M. G., & Piñeiro, G. (2017).
517 The Ecology of Soil Carbon: Pools, Vulnerabilities, and Biotic and Abiotic Controls.
518 *Annual Review of Ecology, Evolution and Systematics*, 48(Volume 48, 2017), 419–445.
519 <https://doi.org/10.1146/annurev-ecolsys-112414-054234>
- 520 Jian, J., Bailey, V., Dorheim, K., Konings, A. G., Hao, D., Shiklomanov, A. N., Snyder, A.,
521 Steele, M., Teramoto, M., Vargas, R., & Bond-Lamberty, B. (2022). Historically inconsis-
522 tent productivity and respiration fluxes in the global terrestrial carbon cycle. *Nature*
523 *Communications*, 13(1), 1733. <https://doi.org/10.1038/s41467-022-29391-5>
- 524 Jian, J., Vargas, R., Anderson-Teixeira, K., Stell, E., Herrmann, V., Horn, M., Kholod, N.,
525 Manzon, J., Marchesi, R., Paredes, D., & Bond-Lamberty, B. (2021). A restructured and
526 updated global soil respiration database (SRDB-V5). *Earth System Science Data*, 13(2),

- 527 255–267. <https://doi.org/10.5194/essd-13-255-2021>
- 528 Jiang, J., Feng, L., Hu, J., Liu, H., Zhu, C., Chen, B., & Chen, T. (2024). Global soil
529 respiration predictions with associated uncertainties from different spatio-temporal data
530 subsets. *Ecological Informatics*, 82, 102777. <https://doi.org/10.1016/j.ecoinf.2024.102777>
- 531 Jobbág, E. G., & Jackson, R. B. (2000). The Vertical Distribution of Soil Organic Carbon
532 and its Relation to Climate and Vegetation. *Ecological Applications*, 10(2), 423–436. [https://doi.org/10.1890/1051-0761\(2000\)010%5B0423:TVDOSO%5D2.0.CO;2](https://doi.org/10.1890/1051-0761(2000)010%5B0423:TVDOSO%5D2.0.CO;2)
- 533 Liu, K., Li, X., Wang, S., & Zhang, H. (2023). A robust gap-filling approach for European
534 Space Agency Climate Change Initiative (ESA CCI) soil moisture integrating satellite
535 observations, model-driven knowledge, and spatiotemporal machine learning. *Hydrology
536 and Earth System Sciences*, 27(2), 577–598. <https://doi.org/10.5194/hess-27-577-2023>
- 537 Luo, Y., Ogle, K., Tucker, C., Fei, S., Gao, C., LaDeau, S., Clark, J. S., & Schimel, D. S. (2011).
538 Ecological forecasting and data assimilation in a data-rich era. *Ecological Applications*,
539 21(5), 1429–1442. <https://doi.org/10.1890/09-1275.1>
- 540 Maier, M., & Schack-Kirchner, H. (2014). Using the gradient method to determine soil gas
541 flux: A review. *Agricultural and Forest Meteorology*, 192–193, 78–95. <https://doi.org/10.1016/j.agrformet.2014.03.006>
- 542 Mariethoz, G., Linde, N., Jougnot, D., & Rezaee, H. (2015). Feature-preserving interpolation
543 and filtering of environmental time series. *Environmental Modelling & Software*, 72, 71–76.
544 <https://doi.org/10.1016/j.envsoft.2015.07.001>
- 545 Marshall, T. J. (1959). The Diffusion of Gases Through Porous Media. *Journal of Soil Science*,
546 10(1), 79–82. <https://doi.org/10.1111/j.1365-2389.1959.tb00667.x>
- 547 Millington, R. J., & Shearer, R. C. (1971). Diffusion in aggregated porous media. *Soil Science*,
548 111(6), 372–378.
- 549 Moffat, A. M., Papale, D., Reichstein, M., Hollinger, D. Y., Richardson, A. D., Barr, A. G.,
550 Beckstein, C., Braswell, B. H., Churkina, G., Desai, A. R., Falge, E., Gove, J. H., Heimann,

- 553 M., Hui, D., Jarvis, A. J., Kattge, J., Noormets, A., & Stauch, V. J. (2007). Comprehensive
554 comparison of gap-filling techniques for eddy covariance net carbon fluxes. *Agricultural and*
555 *Forest Meteorology*, 147(3), 209–232. <https://doi.org/10.1016/j.agrformet.2007.08.011>
- 556 Moldrup, P., Olesen, T., Yamaguchi, T., Schjønning, P., & Rolston, D. E. (1999). Modeling
557 diffusion and reaction in soils: 9. The Buckingham-Burdine-Campbell equation for gas
558 diffusivity in undisturbed soil. *Soil Science*, 164(2), 75.
- 559 National Ecological Observatory Network (NEON). (2024a). *Barometric pressure*
560 (*DP1.00004.001*). National Ecological Observatory Network (NEON). <https://doi.org/10.48443/RT4V-KZ04>
- 562 National Ecological Observatory Network (NEON). (2024b). *Soil CO₂ concentration*
563 (*DP1.00095.001*). National Ecological Observatory Network (NEON). <https://doi.org/10.48443/E7GR-6G94>
- 565 National Ecological Observatory Network (NEON). (2024c). *Soil physical and chemical properties*, *Megapit* (*DP1.00096.001*). National Ecological Observatory Network (NEON). <https://doi.org/10.48443/S6ND-Q840>
- 568 National Ecological Observatory Network (NEON). (2024d). *Soil temperature* (*DP1.00041.001*).
569 National Ecological Observatory Network (NEON). <https://doi.org/10.48443/Q24X-PW21>
- 570 National Ecological Observatory Network (NEON). (2024e). *Soil water content and water*
571 *salinity* (*DP1.00094.001*). National Ecological Observatory Network (NEON). <https://doi.org/10.48443/A8VY-Y813>
- 573 Norman, J. M., Kucharik, C. J., Gower, S. T., Baldocchi, D. D., Crill, P. M., Rayment, M.,
574 Savage, K., & Striegl, R. G. (1997). A comparison of six methods for measuring soil-
575 surface carbon dioxide fluxes. *Journal of Geophysical Research: Atmospheres*, 102(D24),
576 28771–28777. <https://doi.org/10.1029/97JD01440>
- 577 Phillips, C. L., Bond-Lamberty, B., Desai, A. R., Lavoie, M., Risk, D., Tang, J., Todd-Brown,
578 K., & Vargas, R. (2017). The value of soil respiration measurements for interpreting and

- 579 modeling terrestrial carbon cycling. *Plant and Soil*, 413(1), 1–25. <https://doi.org/10.1007/s11104-016-3084-x>
- 580
- 581 Raftery, A. E., Gneiting, T., Balabdaoui, F., & Polakowski, M. (2005). *Using Bayesian Model*
582 *Averaging to Calibrate Forecast Ensembles*. <https://doi.org/10.1175/MWR2906.1>
- 583 Sallam, A., Jury, W. A., & Letey, J. (1984). Measurement of Gas Diffusion Coefficient under
584 Relatively Low Air-filled Porosity. *Soil Science Society of America Journal*, 48(1), 3–6.
585 <https://doi.org/10.2136/sssaj1984.03615995004800010001x>
- 586 Shao, J., Zhou, X., Luo, Y., Li, B., Aurela, M., Billesbach, D., Blanken, P. D., Bracho, R.,
587 Chen, J., Fischer, M., Fu, Y., Gu, L., Han, S., He, Y., Kolb, T., Li, Y., Nagy, Z., Niu, S.,
588 Oechel, W. C., ... Zhang, J. (2015). Biotic and climatic controls on interannual variability
589 in carbon fluxes across terrestrial ecosystems. *Agricultural and Forest Meteorology*, 205,
590 11–22. <https://doi.org/10.1016/j.agrformet.2015.02.007>
- 591 Shao, P., Zeng, X., Moore, D. J. P., & Zeng, X. (2013). Soil microbial respiration from
592 observations and Earth System Models. *Environmental Research Letters*, 8(3), 034034.
593 <https://doi.org/10.1088/1748-9326/8/3/034034>
- 594 Sih, D., Gerber, S., Inglett, P. W., & Inglett, K. S. (2016). Comparing models of microbial–
595 substrate interactions and their response to warming. *Biogeosciences*, 13(6), 1733–1752.
596 <https://doi.org/10.5194/bg-13-1733-2016>
- 597 Tang, J., Baldocchi, D. D., Qi, Y., & Xu, L. (2003). Assessing soil CO₂ efflux using continuous
598 measurements of CO₂ profiles in soils with small solid-state sensors. *Agricultural and Forest*
599 *Meteorology*, 118(3), 207–220. [https://doi.org/10.1016/S0168-1923\(03\)00112-6](https://doi.org/10.1016/S0168-1923(03)00112-6)
- 600 Tang, J., Misson, L., Gershenson, A., Cheng, W., & Goldstein, A. H. (2005). Continuous
601 measurements of soil respiration with and without roots in a ponderosa pine plantation
602 in the Sierra Nevada Mountains. *Agricultural and Forest Meteorology*, 132(3), 212–227.
603 <https://doi.org/10.1016/j.agrformet.2005.07.011>
- 604 Taylor, J. R. (2022). *An Introduction to Error Analysis: The Study of Uncertainties in Physical*

- 605 *Measurements, Third Edition* (3rd ed.). University Science Press.
- 606 Yan, Z., Bond-Lamberty, B., Todd-Brown, K. E., Bailey, V. L., Li, S., Liu, C., & Liu, C. (2018).
- 607 A moisture function of soil heterotrophic respiration that incorporates microscale processes.
- 608 *Nature Communications*, 9(1), 2562. <https://doi.org/10.1038/s41467-018-04971-6>
- 609 Yan, Z., Liu, C., Todd-Brown, K. E., Liu, Y., Bond-Lamberty, B., & Bailey, V. L. (2016).
- 610 Pore-scale investigation on the response of heterotrophic respiration to moisture conditions
- 611 in heterogeneous soils. *Biogeochemistry*, 131(1), 121–134. <https://doi.org/10.1007/s10533-016-0270-0>
- 613 Zhang, R., Kim, S., Kim, H., Fang, B., Sharma, A., & Lakshmi, V. (2023). Temporal
- 614 Gap-Filling of 12-Hourly SMAP Soil Moisture Over the CONUS Using Water Balance
- 615 Budgeting. *Water Resources Research*, 59(12), e2023WR034457. <https://doi.org/10.1029/2023WR034457>